UC San Diego
UC San Diego Previously Published Works

Title

The Importance of Remote Forcing for Regional Modeling of Internal Waves

Permalink

https://escholarship.org/uc/item/4jf6318z

Journal

Journal of Geophysical Research - Oceans, 125(2)

ISSN

2169-9275

Authors

Mazloff, Matthew R
Cornuelle, Bruce
Gille, Sarah T
et al.

Publication Date

2020-02-01

DOI

10.1029/2019jc015623

Peer reviewed

The Importance of Remote Forcing for Regional Modeling of Internal Waves

Matthew R. Mazloff[1] , **Bruce Cornuelle[1]** , **Sarah T. Gille[1]** , and **Jinbo Wang[2]**

[1]Scripps Institution of Oceanography, University of California, San Diego, La Jolla, CA, USA, [2]Jet Propulsion Laboratory, California Institute of Technology, Pasadena, CA, USA

Abstract Regional ocean general circulation models are generally forced at the boundaries by mesoscale ocean dynamics and barotropic tides. In this work we provide evidence that remotely forced internal waves can be a significant source of energy for the dynamics. We compare global and regional model solutions within the California Current System. Both models have similar inputs, forcings, and identical grids and numerics. The global model has a steric height power spectrum consistent with mooring observations at superinertial frequencies, while the regional model spectrum is weaker. The regional model also has less sea surface height variance at high wavenumber than the global model. The vertical velocity variance is significantly larger in the global model, except in the sheltered Southern California Bight. While the regional model has roughly equal high-pass baroclinic and barotropic kinetic energy levels, the global model high-pass baroclinic kinetic energy is 28% (0.39 PJ) greater than the barotropic energy. An internal wave energy flux analysis reveals that the regional model domain boundaries act as a sink of 183 MW, while in the global model the analysis domain boundaries act as a source of 539 MW. This 722 MW difference can account for the relative increase of 0.39 PJ high-pass baroclinic energy in the global model, assuming a baroclinic kinetic energy dissipation time in the domain of approximately 6.3 days. The results here imply that most regional ocean models will need to account for internal wave boundary fluxes in order to reproduce the observed internal wave continuum spectrum.

Plain Language Summary Global ocean simulations can be too computationally expensive, so many researchers prefer to use lower cost regional ocean models. The open ocean boundary conditions of these regional models must be prescribed from other products. It is common practice for these prescribed conditions to lack high-frequency oceanic variability. Here we show that this missing component of the dynamics may account for a large amount of the overall high-frequency energy in the region. Without this, remotely forced energy input regional models may underestimate processes important to the overall state (e.g., upwelling processes fundamental to the ocean ecosystems). Regional models must account for these remotely forced dynamical signals in order to produce simulations with realistic short time- and space-scale variability.

1. Introduction

Computational expense limits our ability to simulate and assimilate submesoscale and internal wave dynamics in global ocean models. However, observations at these scales are becoming more abundant due to growing capabilities for both in situ and remote sensing measurements. Moreover, there is a demand for hindcasts and forecasts at these scales. One pressing need is the capability to estimate the sea surface height (SSH) at 10 km scales during the Surface Water and Ocean Topography (SWOT) altimeter calibration and validation mission (Morrow et al., 2019; Wang et al., 2018). To efficiently reproduce observed submesoscale and internal wave dynamics, we look to regional models, in which we can afford to resolve these scales.

A prerequisite for assimilating internal wave and submesoscale information is the ability of the model to represent these dynamics. Critical phenomena occurring outside the regional domain and then propagating in must be prescribed (i.e., forced) at the domain "open" horizontal boundaries. Much work has gone into the handling (e.g., Marchesiello et al., 2001; Marsaleix et al., 2006) and optimization (e.g., Hoteit et al., 2005) of open boundary forcing for the mesoscale circulation in regional models. Efforts to force shorter time scales (e.g., superinertial, with frequencies greater than approximately 1 cycle per day), however, have thus far received little attention.

The observed continuum spectrum of internal wave energy (Garrett & Munk, 1975) is fed largely from tidal forcing, wind forcing, and the large-scale circulation (Ferrari & Wunsch, 2010). One expects near-tidal internal wave energy to be proportional to barotropic tidal energy, as the conversion is theorized to scale linearly (Jayne & St. Laurent, 2001). Barotropic tides generate internal tides via interaction with bottom topography. Modeling the spread of this energy and achieving the observed continuum spectrum requires simulating the internal tides with sufficient grid spacing to resolve the nonlinear interactions among waves and eddies and with sufficient duration for the energy to spread in frequency space (Polzin, 2004). Therefore, while regional models excite near-inertial waves and internal tides within their domains, they will not achieve a realistic continuum spectrum if the internal tide residence time is too short to develop a nonlinear wave-wave and wave-eddy equilibrium.

Similarly, regional models must have a domain size large enough to encompass a sufficient amount of internal tide generation. Ponte and Cornuelle (2013) tested the influence of model domain size on tidal simulations. They generated internal M2 and K1 tides by forcing at the open boundaries with M2 and K1 barotropic tides. As they increased the domain size of their regional model the equilibrium internal tide energy also kept increasing. This was true up to the largest domain size they considered, which was 1,024 km × 1,024 km. The larger domains included more topographic features capable of generating M2 and K1 internal tides.

In this paper we provide evidence that internal wave energy propagation through regional model open boundaries must be accounted for to achieve the observed internal gravity wave continuum spectrum. This is the case even if the regional model domain contains realistic topography capable of generating internal tides. Section 2 presents the models and data used in this study. Comparisons of the models and observations are presented in section 3, which concludes with an assessment of the internal wave energy flux across the boundaries of the analysis domain for both the global and regional models. A concluding discussion is given in section 4

2. Model and Observational Resources

This study analyzes a global and two regional models. Observations are from moorings, tide gauges, and altimeters. This section describes these resources.

2.1. Models
2.1.1. Global MITgcm: LLC4320
In order to assess the role of internal wave-related processes generated in a global domain, we analyze the 1 June to 30 September 2012 simulation from the Latitude-Longitude-polar Cap "LLC4320" MITgcm setup (available at https://data.nas.nasa.gov/dataset/5). This global model has nominally 1/48° horizontal grid spacing; in the California Current region the LLC4320 has approximately 1.8 km grid spacing. There are 90 vertical levels of varying thickness, with 1 m spacing at the surface telescoping to much coarser with depth. The model uses z coordinates with partial cells (Adcroft et al., 1997), and bathymetry is derived from ETOPO-5. The primitive equations are solved on an Arakawa C grid, using a multidimensional seventh-order one-step method with monotonicity preserving limiter for temperature and salinity advection (Daru & Tenaud, 2004). Horizontal viscosity is parameterized using a modified Leith scheme (Fox-Kemper & Menemenlis, 2013). There is no explicit horizontal diffusivity. Vertical viscosity and diffusivity are determined from the K-profile parameterization (Large et al., 1994). A quadratic bottom drag is prescribed with a drag coefficient of 0.0021. This simulation has been described in several recent studies (e.g., Chereskin et al., 2019; Flexas et al., 2019; Qiu et al., 2018, 2020; Savage et al., 2017; Su et al., 2018; Torres et al., 2018; Wang et al., 2019). Chereskin et al. (2019) conduct a model-observation comparison showing that the upper ocean properties are realistic in this region. Similarly, Rocha et al. (2016) show that model statistics are consistent with Acoustic Doppler Current Profiler measurements in the Drake Passage. The MITgcm options used in this run can be found online (at http://wwwcvs.mitgcm.org/viewvc/MITgcm/MITgcm_contrib/llc_hires/llc_4320/). The MITgcm has been used in numerous studies of tidal dynamics and interactions (e.g., Flexas et al., 2015; Hughes & Klymak, 2019; Klymak et al., 2016; Musgrave et al., 2016; Nikurashin & Legg, 2011). We note, however, that this LLC4320 simulation, which prescribed the lunisolar tides as a pressure loading force at the sea surface (as described in Arbic et al., 2018), had a mistake in the implementation resulting in the forcing being approximately 11% too strong. The impacts of this are discussed below.

2.1.2. Regional MITgcm

The regional MITgcm setup is derived from the LLC4320 setup. It uses the same MITgcm configuration options and grid, with four differences of note. The first difference is that the regional model time step is 150 s instead of 25 s, though sensitivity tests found that this does not impact the solution (not shown). The second difference is that the regional model uses the fifth generation of European Centre for Medium-Range Weather Forecasts atmospheric reanalyses (ERA5) instead of the ERA-Operational (ERA-O) atmospheric state used in LLC4320 (ERA data available at Copernicus Climate Change Service https://cds.climate.copernicus.eu/cdsapp#!/home). ERA5 is higher resolution and provides hourly instead of 3-hourly fields, implying that the ERA5 atmospheric state would be expected to impart more energy into the regional ocean model than ERA-O imparts to the global model. The third difference is the bathymetry is slightly different, having been updated from ETOPO5 to a bathymetry derived by blending ETOPO1 (Amante & Eakins, 2009) and a product from the Southern California Coastal Ocean Observing System (Divins & Metzger, 2008). The fourth difference is, obviously, that the regional model has open boundary conditions. These are prescribed from 7-day global Hybrid Coordinate Ocean Model + Navy Coupled Ocean Data Assimilation (HYCOM+NCODA) output (https://www.hycom.org/) at the edge of the model domain and restored to the HYCOM+NCODA values over the next 10 grid cells with a time scale linearly scaling from 12 hr to 10 days. The analysis domain begins at the edge of this 10-cell restoring layer (i.e., we begin our analysis on the eleventh model grid cell). Barotropic tides are prescribed using eight equilibrium tide constituents from the TPXO7 product (Egbert & Erofeeva, 2002) as a volume transport at the outer edge of the model domain. A local tidal forcing is also prescribed at the surface via a pressure loading field derived using astronomical inputs from the NASA's Navigation and Ancillary Information Facility and the NASA SPICE toolkit (Acton et al., 2018), with code for generating this field available online (at https://github.com/joernc/tidal-potential). The bias in the tidal loading forcing prescribed in the LLC4320 simulation is not present in these forcing fields.

The MITgcm regional model is initialized from HYCOM+NCODA 1 January 2015. We consider 2015 a spin-up year; the domain kinetic energy has reached an equilibrium by 2016 (not shown). To match the analysis time of year with the global model, we focus on analyzing 1 June 2016 to 30 September 2016. Thus, the years are different for LLC4320 and the regional model, but the same number of time records are analyzed, and the same span of the seasonal cycle is assessed. We show later that though there is significant interannual variability at low frequency, the high-frequency interannual variability is insignificant.

2.1.3. Regional ROMS

To further investigate regional model statistics, we analyze a Regional Ocean Model System (ROMS) simulation produced at the Jet Propulsion Laboratory by Zhijin Li (Li et al., 2019). The ROMS regional model setup comprises an outer domain with 9 km grid spacing (L0), a one-way nested intermediate domain with 3 km grid spacing (L1), and an additional one-way nested inner domain run with 1 km grid spacing (L2). The L1 domain size is similar to the MITgcm analysis domain shown in Figure 1, and the L2 domain has similar longitudinal extent (out to 128°W), but the latitudinal extent is only from about 34.5°N to 39°N. The atmospheric forcing is derived from bulk formula (Fairall et al., 2003) using hourly atmospheric state from the 4-km resolution version of the Coupled Ocean/Atmosphere Mesoscale Prediction System (COAMPS) operated by the Naval Research Laboratory (Hodur, 1997). The K-profile parameterization (Large et al., 1994) was used for the boundary layer turbulent mixing. The boundary condition of the L0 domain uses the Met Office Hadley Centre "EN4" product (Good et al., 2013). Barotropic tidal forcing was prescribed along the L1 boundaries using the Oregon State University Inverse Tidal Software (OTIS, Egbert & Erofeeva, 2002). The steric height used in the model-data comparison of this study is derived from the L2 domain. This is a shorter run at a different period in the year, so we use this run only in the mooring comparison to assess whether the regional model issues are model dependent. Li et al. (2019) provide more details on the model setup.

2.2. Data

2.2.1. MBARI-M2 Mooring

The "MBARI-M2" mooring (WMO platform code 46093) data were collected and made freely available by the Monterey Bay Aquarium Research Institute. This mooring is located at 36.69623°N, 122.3997°W (Figure 1). Temperature and salinity data analyzed from this mooring are from 1 June to 30 September in 2009 at nominal depth levels of 1, 10, 20, 40, 60, 80, 100, 150, 200, 250, and 300 m. The data are available online (at http://dods.mbari.org/data/ssdsdata/deployments/m2/).
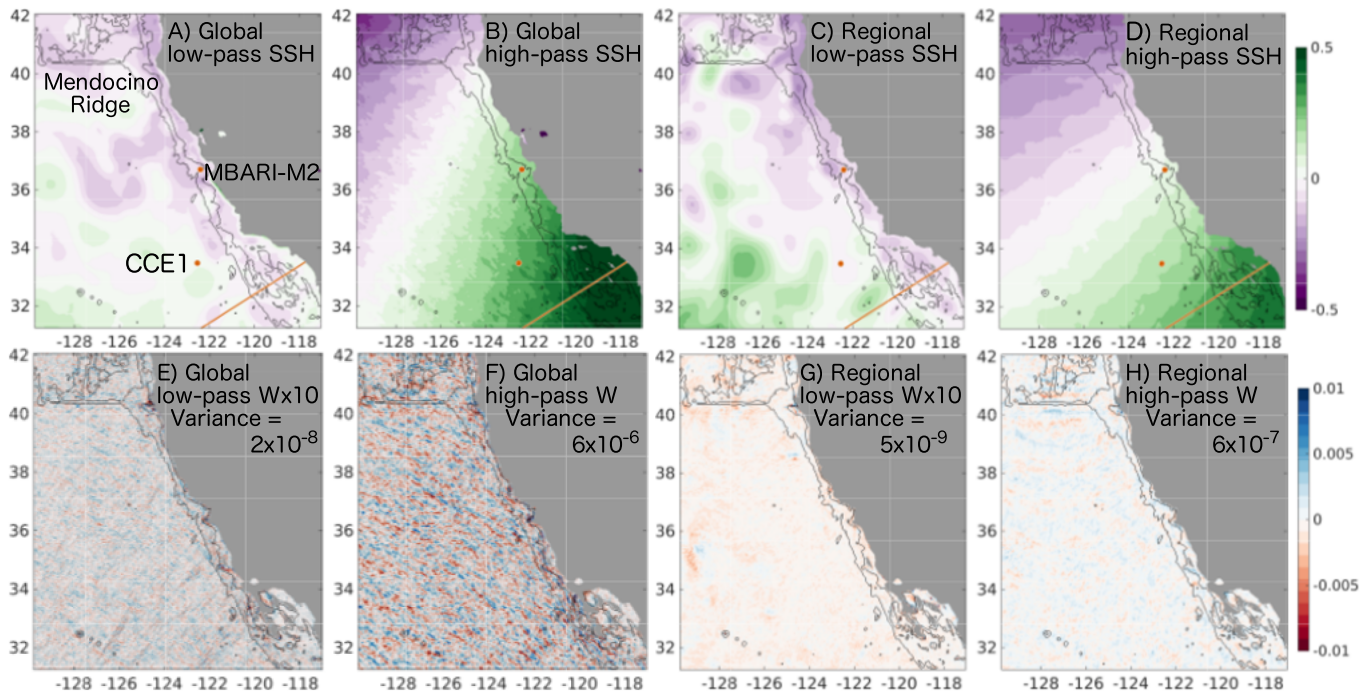
Figure 1. A snapshot on 2 June of temporally low-pass and high-pass filtered (using 24-hr running mean) SSH (m) (a–d) and vertical velocity (m/s) at 500 m (e–h) from the global model (a, b, e, f) and regional model (c, d, g, h). The location of the MBARI-M2 mooring and the CCE1 mooring are denoted with orange circles in the top plots. The orange line denotes the California Cooperative Oceanic Fisheries Investigations (CalCOFI) line 90, which serves as a standard reference transect for ocean sampling. The black contour denotes the 1,000 and 3,000 m isobath. The Mendocino Ridge is pointed out in a. Note that the low-pass vertical velocity has been multiplied by 10 such that it can be plotted using the same color scale as the high-pass vertical velocity. The spatial variance of the vertical velocity field is noted in panels e–h.

2.2.2. CCE1 Mooring

The California Current Ecosystem (CCE) mooring data were collected by the Scripps Institution of Oceanography under a grant from the Climate Observation Division, Climate Program Office, National Oceanic and Atmospheric Administration, U.S. Department of Commerce. The CCE1 mooring is located at 33.45°N, 122.5167°W (Figure 1). Temperature and salinity data analyzed from this mooring are from 1 June to 30 September in 2016 and 2017 at nominal depth levels of 9, 19, 29, 39, 60, 75, 150, and 301 m. These data are available online (at http://mooring.ucsd.edu/index.html?CCE).

2.2.3. Altimetry

SSH data from the California Current region are taken from exact-repeat altimeter measurements collected by the Jason-1, Jason-2, AltiKa, and Sentinel-3 radar altimeters. We use the same approach adopted by Chereskin et al. (2019) to select altimeter ground tracks and compute along-track wavenumber spectra. Our objective is to infer small spatial scale statistics at which internal wave processes are potentially important.

The ability of a nadir altimeter to resolve high-wavenumber processes depends on the satellite footprint size (the size of the region that is averaged together to obtain a single reported measurement) as well as the frequency at which data are reported. The Jason-1 and Jason-2 altimeters have footprints of 10-km radius (e.g., Dibarboure & Morrow, 2016) and report data at 20 Hz, corresponding to a Nyquist wavenumber of 1 cycle per 0.5 km. For Jason-1 and Jason-2, we use data that have been retracked with the Adaptive Leading Edge Subwaveform algorithm (Passaro et al., 2016), which was designed to meet the small-scale requirements of coastal altimetry. AltiKa has a smaller footprint, about 4 km in radius (e.g., Verron et al., 2018), and reports data at 40 Hz (i.e., a Nyquist wavenumber of about 1 cycle per 0.25 km). Sentinel-3 has an even smaller footprint, 1.5 km or less in radius (e.g., Bonnefond et al., 2018), but its orbit differs from those of the TOPEX/Jason and ERS-1-2/Envisat/AltiKa series of altimeters, so the mean sea surface is less well constrained along its ground track. At scales from about 10–50 km, the AltiKa and Jason altimeters show a nearly white spectrum, sometimes identified as a spectral bump. This has been attributed to preferential radar returns from isolated regions within the satellite footprint (e.g., Dibarboure et al., 2014). Vergara et al. (2019) removed background noise from their spectra in order to reduce the impact of white noise at scales of

about 70 km and shorter. We have not adopted their noise removal approach, and to avoid the risk of over-interpreting signal noise, we focus our discussion on the red portion of the spectrum, at scales larger than 70 km.

3. Results

To evaluate the dynamical scales of the global and regional MITgcm simulations, we separate the high-frequency and low-frequency components of the model solutions using a 24-hr running mean. A snapshot of the high-pass and low-pass components of SSH and vertical velocity, w, at 500 m (Figure 1) reveals similarities in the regional and global SSH. The low-pass SSH for both models (Figures 1a and 1c) shows a prominent cross-shelf gradient in SSH (with high SSH offshore and low SSH onshore), characteristic of the California Current System. This large-scale pattern is modulated by mesoscale eddy features. The high-pass SSH has a similar range of values (Figures 1b and 1d) but reflects the large-scale barotropic tide, which propagates north-south along the coastline. Small-scale internal wave features are also noticeable in the global model high-pass SSH (Figure 1b).

The vertical velocity, w, is strongly dependent on internal-wave-induced motions. The high-pass w is significantly larger than the low-pass w in both the regional and global model (Figures 1e–1h). The low-pass w was multiplied by a factor of 10 (Figures 1e and 1g) so that it could be plotted using the same color scale axis as the high-pass w (Figures 1f and 1h). The most striking differences between the global and regional models appear in high-pass w, which shows significantly greater variance in the global model (Figure 1f) than in the regional model (Figure 1h). An animation of the vertical velocity at 500 m in both runs is provided as supporting information and for the global model shows high-frequency waves propagating into the domain and ending on the coast. The animation suggests the differences may arise from remotely generated fluxes in the global model. The objectives of this analysis are to explore the origins of these differences in w magnitude and to probe the attenuated small-scale SSH structure in the regional model.

3.1. Validation of Tidal Forcing in the Simulations Using Tide Gauges

As can be seen in high-pass SSH (Figures 1b and 1d), barotropic tides are a primary component of high-frequency dynamical forcing. We compare the regional and global model SSH to three tide gauges in the Southern California Bight (SCB). The years analyzed differ for the two runs, but the yeardays are identical (i.e., 1 June to 30 September). The amplitudes and phases derived using a standard tide harmonic analysis code (T_TIDE, Pawlowicz et al., 2002) for the five largest tidal components are shown in Table 1. The semidiurnal lunar M2 tidal component is dominant, with an amplitude of ~0.5 m. Compared to the tide gauges, the global model overestimates this by about 25% to 35%, which, as stated above in section 2.1.1, has been previously diagnosed and attributed to biases in the prescribed forcing. Meanwhile the regional model, which does not have this bias in the prescribed tidal forcing, underestimates the M2 amplitude by about 9% to 15%. For the next largest constituent, K1 (lunar diurnal), the global model has a very similar amplitude that is only a few percent lower than the gauges, while the regional model K1 amplitude is about 16% larger than the gauges. The comparisons for the next three largest tidal constituents are similar, with the O1 (also lunar diurnal) being slightly low in the global model and slightly high in the regional model. The S2 (solar semidiurnal) is significantly higher in the global model, and slightly lower in the regional model. The N2 (larger lunar elliptic semidiurnal) component is consistent across both models and gauges, with all showing an amplitude of approximately 0.1 m. To summarize, both models simulate the tides with amplitude differences from the tide gauges of less than 35%. However, the global model M2 amplitude averages 0.657 m for the three tide gauge locations, while the regional amplitude mean is 31% lower at 0.451 m, which is closer to the observations.

For fixed topography and stratification, internal tide generation is proportional to the amplitude of the barotropic tide (Jayne & St. Laurent, 2001). Thus, one expects the total internal tidal energy to scale with the sum of the squared propagating barotropic tidal component amplitudes. (Values are squared because energy goes as the square of velocity.) The global to regional tidal amplitude ratios vary significantly for each component and tide gauge location (far right column in Table 1). The total energy will reflect the regional average tidal energies and ratios. For the dominant constituent, M2, the global to regional amplitude ratio is about 1.5, suggesting the locally generated internal M2 tidal energy is expected to be approximately 2.3 (i.e., 1.5^2) times larger in the global model.

Table 1
Global and Regional Models Compared to Three Tide Gauges in the SCB

Tide gauges	Gauge (2012) amplitude	Gauge phase	Global amplitude	Global phase	Gauge (2016) amplitude	Gauge phase	Regional amplitude	Regional phase	Ratio global to regional
Harvest station									
M2	0.481	162	0.605	152	0.487	165	0.453	179	1.34
K1	0.332	215	0.323	227	0.320	227	0.367	233	0.88
O1	0.207	210	0.149	243	0.180	196	0.227	213	0.66
S2	0.151	162	0.286	193	0.148	161	0.117	180	2.44
N2	0.106	133	0.088	122	0.106	141	0.101	153	0.87
Santa Barbara									
M2	0.507	155	0.665	148	0.514	157	0.458	174	1.45
K1	0.341	213	0.330	226	0.324	225	0.373	232	0.88
O1	0.212	208	0.155	242	0.185	194	0.231	212	0.67
S2	0.174	155	0.311	188	0.168	155	0.130	173	2.39
N2	0.111	128	0.095	119	0.110	136	0.105	148	0.90
Santa Monica									
M2	0.517	146	0.700	141	0.526	148	0.443	165	1.58
K1	0.329	209	0.324	222	0.314	221	0.366	229	0.89
O1	0.206	205	0.155	237	0.180	191	0.225	210	0.69
S2	0.196	147	0.327	179	0.191	147	0.137	162	2.39
N2	0.113	119	0.103	113	0.113	128	0.102	141	1.01

Note. These calculations are all for 1 June to 30 September, but the global model comparison is in 2012 and the regional model comparison is for 2016. Amplitude is in meters.

3.2. Comparisons to Mooring

The last subsection showed that the forced barotropic tidal constituents in the global and regional MITgcm runs have amplitudes within 35% of observations. To evaluate the baroclinic component, we compare the steric height in the upper 300 m in the models to mooring timeseries. The choice to look at steric height is motivated both by the noticeable differences in the high-pass SSH in Figure 1 and by its relevance to future high-resolution altimetry missions (e.g., SWOT). The model runs and mooring output are for different years, but, as in the tidal analysis, for each run we begin with the same yearday of 1 June. To assess whether interannual variability is an issue, the CCE1 mooring is analyzed in both 2016 and 2017. The low-frequency behavior in these two years is significantly different (Figure 2), but differences in the high-frequency energy in the two years are undetectable. Differences in the high-frequency energy between the mooring time series and the global LLC4320 model are also insignificant. However, the regional model lacks high-frequency energy. The forced barotropic tidal peaks and their harmonics are apparent, but the energy between these bands is missing.

To ensure that the results from the CCE1 mooring are robust, we also consider the MBARI-M2 mooring. We find consistent results: while the high-frequency energy in the mooring and global model are comparable, the MITgcm regional model significantly underestimates the energy. For this location we also have output from the ROMS regional model. Comparison shows the ROMS model high-frequency spectrum to be only slightly closer to the observations than the MITgcm regional model. The only significant difference between the MITgcm simulations is the domain size (i.e., global versus regional), while the ROMS model differs from the global MITgcm simulation in numerous ways. However, the fact that the regional ROMS model is more similar to the regional MITgcm model than to either the global model or the mooring suggests that the missing energy is associated with being a regional model.

3.3. Comparisons of Wavenumber Spectra From Altimetry

In addition to frequency spectra, we also use wavenumber spectra of SSH as a metric to evaluate model behavior. For satellite altimetery, at scales longer than about 50–70 km, SSH spectra are red with a spectral slope of about k^{-2} (Figure 3). Spectra flatten out at scales shorter than ~50 km but will not be discussed
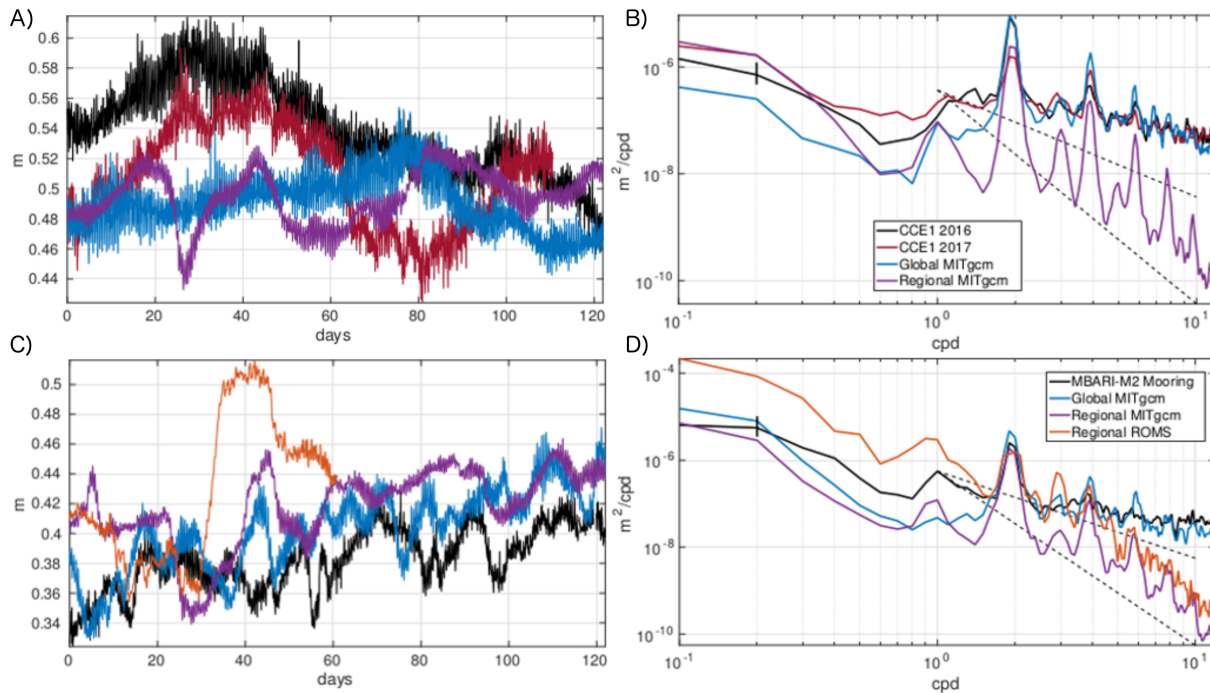
Figure 2. Comparison of steric height in the upper 300 m from mooring observations, a global model, and regional models. (a) Time series and (b) power spectra density comparison to the CCE1 mooring. (c) Time series and (d) power spectra density comparison to the MBARI-M2 mooring. Mooring locations denoted in Figure 1. The dashed lines in b and d denote a slope of −2 and −4.

here. At scales longer than about 100 km, wavenumber spectra from model and altimeter are roughly consistent. However, at scales shorter than ~100 km the model spectra have much lower energy than altimeter spectra: this may be attributed both to the spectral energy in the altimeter data associated with altimeter noise and to lower energy in the models associated with diffusive processes used to approximate the effects of subgrid-scale physics.

Compared to the regional model, the global model has more energy at wavelengths shorter than 70 km. The excess energy can be attributed to high-frequency internal waves: Rocha et al. (2016) showed that the extra energy could be suppressed by daily averaging the data to remove motions on scales shorter than the diurnal frequency, including suppressing inertial motions. In this case, for scales shorter than about 70 km the daily averaged global model solution (dashed green line in Figure 3) shows less energy and better resembles the regional model (magenta line). This is consistent with the hypothesis that the regional model is missing short scale energy at high-frequency, as also suggested from the high-frequency SSH plot of Figure 1.

3.4. Statistics in the Domain
Motivated by the high-frequency vertical velocity magnitude difference apparent in Figure 1, we plot the w variance at 500 m for the global and regional MITgcm over 122 days starting 1 June (Figure 4). In both models there is larger variance near complex bathymetry, especially the Mendocino Ridge, but at 500 m depth the global model w variance is on average 7 times larger than the regional. Figure 4c plots the ratio of w variance (regional divided by global). The animation included in the supporting information also illustrates the difference between 500 m w fields in the two models.

One location where the variance of w is more similar in the global and regional models is in the SCB (~ 33°N, 119°W in Figures 4a and 4b). Figure 4c shows that in the most sheltered regions, the variance ratio approaches unity. To make a clear comparison at three locations (marked with red dots in Figure 4c), we plot the standard deviation of w as a function of depth for the global and regional models. Near the surface w is damped in both models due to higher stratification and the surface boundary condition. Similarly, w approaches zero at the ocean floor due to the bottom boundary condition. In the open ocean (points P1 and P2 in Figure 4c) interior depths the w standard deviation is several times larger in the global model than the regional model (green and blue lines in Figure 4d). However, at the point in the SCB (P3, red lines in
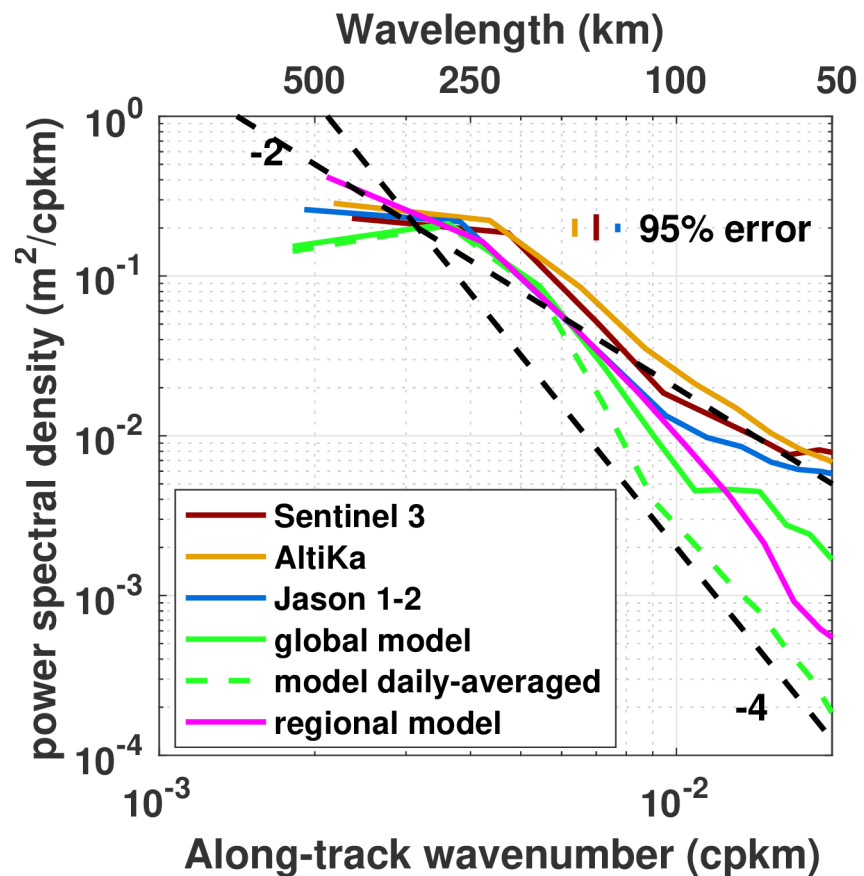
Figure 3. Wavenumber spectra for sea surface height, comparing the MITgcm regional model (magenta), the global MITgcm (green), and three nadir altimeter products selected for their capabilities to resolve smaller-scale sea surface height variability (see text), adapted from Chereskin et al. (2019). Model fields are computed along CalCOFI line 90, indicated in orange in Figure 1. Vertical lines indicate 95% significance levels for the altimeter spectra.

Figure 4d), the differences in w variability are smaller, even though the chosen point is less shielded than the northern SCB.

The heightened w variance in the global model is consistent with the hypothesis that remotely generated internal waves freely propagate into the region to enhance variability. However, these waves are attenuated in the SCB as they interact with the Santa Rosa Ridge (location noted in Figures 4a and 4b). Enhanced mixing associated with this ridge has been observed (Johnston & Rudnick, 2015; Kilpatrick et al., 2018; Rudnick et al., 2017) and is likely associated with internal wave scattering and breaking.

3.5. Domain Energetics

Analyzing the domain baroclinic and barotropic kinetic energy content provides information about the cause of the global and regional model differences. To isolate the high-pass baroclinic energy, we consider the zonal, meridional, and vertical velocities. The vertically averaged component of the zonal and meridional velocities are first removed from every hourly snapshot. We then high-pass filter the velocity components by removing a 24-hr running mean. The high-pass baroclinic velocities are squared and summed and multiplied by $\rho_o/2$ (producing a baroclinic kinetic energy in units of joules per unit volume). The vertical integral of these fields is significantly larger in the global model (Figure 5). Integrating over the whole analysis domain yields a total high-pass baroclinic kinetic energy of 1.79 ± 0.22 PJ in the global model and 0.71 ± 0.10 PJ in the regional model, a difference of 1.08 PJ. Conversion from low-frequency energy cannot account for this difference, as the total baroclinic kinetic energy is similar in the global model (3.49 ± 0.24 PJ) and in the regional model (3.60 ± 0.28 PJ).

The total high-pass barotropic energy in the global run is 1.40 PJ, which is approximately double the regional run inventory of 0.71 PJ (Figure 6a). However, almost all of this energy is in the M2 band, which accounts
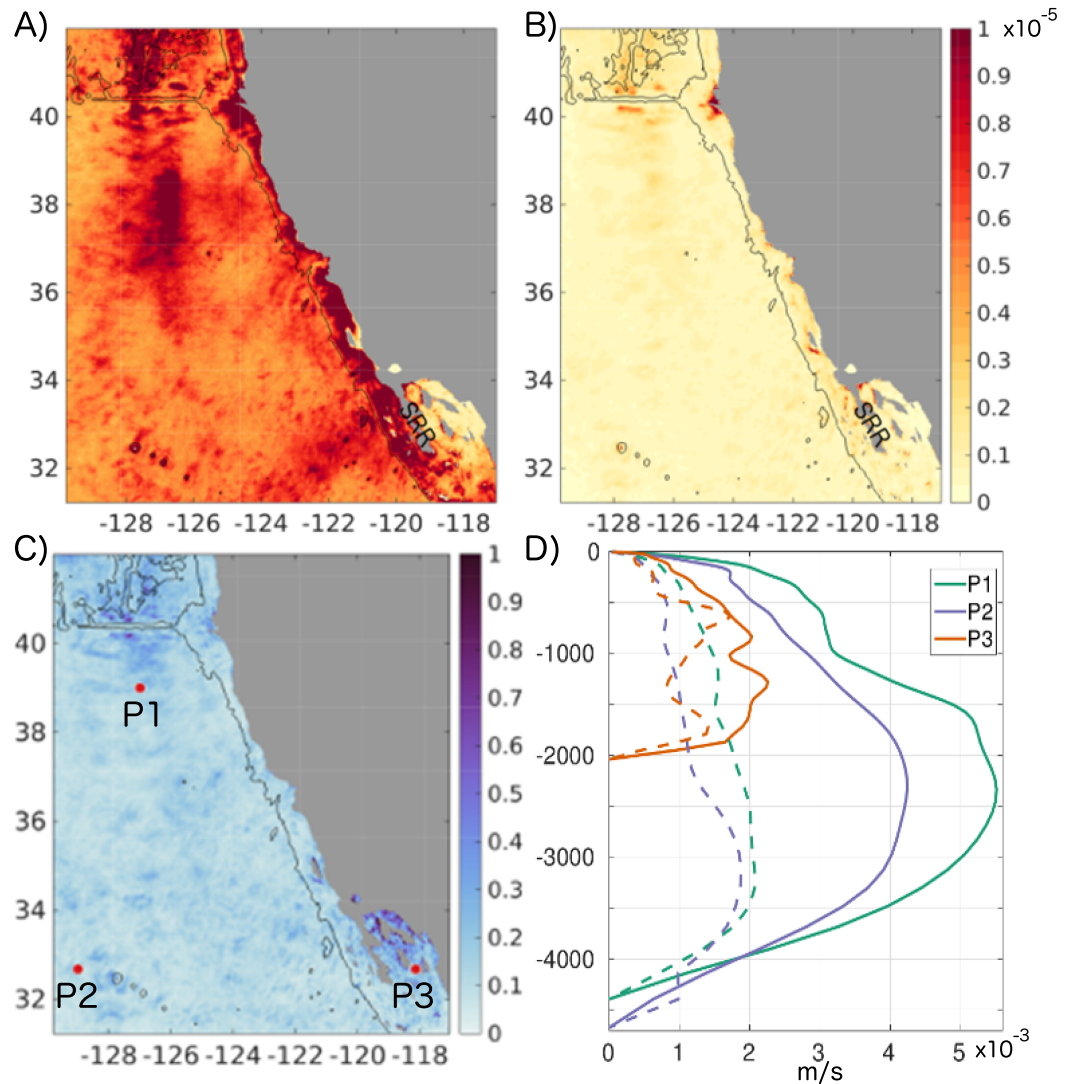
Figure 4. Variance of vertical velocity, w, at 500 m from (a) global and (b) regional configurations of the MITgcm, and (c) their ratio (regional divided by global). The 3,000 m bathymetry contour is in black. The location of the Santa Rosa Ridge (SRR) is noted in panels a and b. Three points are denoted in c: P1 is near the Mendocino Ridge, P2 is in the analysis domain southwest corner, and P3 is inside the Southern California Bight. Panel d shows the vertical profiles of w standard deviation at these three locations for the global (solid lines) and regional (dashed lines) models.

for 1.33 PJ in the global run and 0.57 PJ in the regional run. Thus, this difference in barotropic energy is explained by the tidal analysis presented in section 3.1, where we showed that the forced M2 is approximately 1.5 times larger in the global model. Thus, one expects approximately $1.5^2 = 2.25$ times the barotropic energy, which is consistent with the M2 energy ratio $1.33/0.57 = 2.33$.

Time series of the spatially integrated high-pass barotropic and baroclinic energy are shown in Figure 6, with variability largely reflecting the spring/neap tide. The variability in the baroclinic energy is strongly lag correlated with the barotropic M2 tidal band energy. The lag correlation peaks at 1.9 days for the global model and 2.8 days for the regional model. This correlation implies barotropic M2 energy is being converted to baroclinic energy, which is expected to occur when the barotropic tide interacts with topography (Jayne & St. Laurent, 2001). Given that the global and regional models have the same numerics and topography, one might assume that the total barotropic to baroclinic conversion rate will be equivalent in the two domains. However, while the regional MITgcm model has equal partition between high-frequency barotropic and baroclinic energy (0.71 PJ), the global model shows higher energy in the high-frequency baroclinic component (1.79 PJ) than in the barotropic component (1.40 PJ). Given the numerous contributions to the
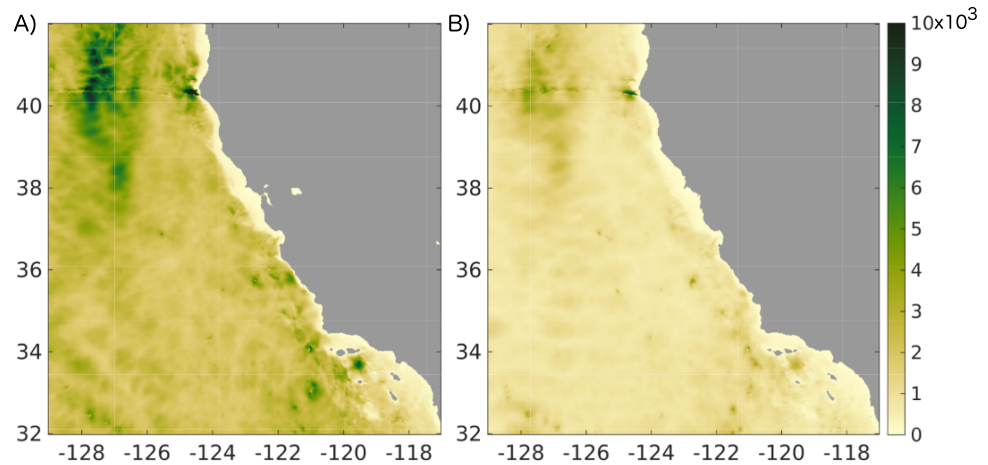
Figure 5. The vertically integrated high-pass baroclinic kinetic energy per unit volume (J m^{-2}) for (a) global and (b) regional MITgcm runs. The total high-pass baroclinic energy in the domain is 1.79 PJ for the global model and 0.71 PJ for the regional model.

high-pass baroclinic energy budget there is no reason to expect a one-to-one relationship between barotropic and baroclinic energy found in the regional domain. However, given the identical numerics in both domains it is unlikely that the local conversion rate could be 28% larger in the global domain, making one question the source of this 0.39 PJ difference between barotropic and baroclinic components in the global model.

3.6. Energy Flux Through the Analysis Domain Boundaries

The global and the regional MITgcm simulations have the same grid and numerical schemes. They have similar bathymetry, atmospheric forcing, and barotropic tidal forcing. Nevertheless, the high-frequency energy in the global model is significantly larger everywhere, with the only exception being in the most sheltered parts of the SCB. We find the domain integrated high-pass barotropic and baroclinic energy levels in the
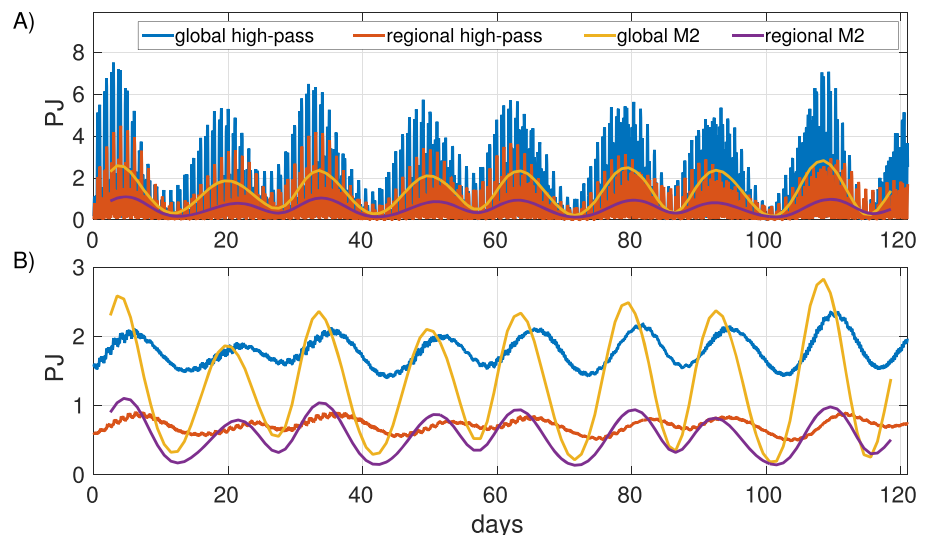

Figure 6. (a) The barotropic high-pass kinetic energy in the global (blue line) and regional (red line) models. The barotropic kinetic energy at the M2 frequency is also plotted for the global (yellow line) and regional (purple line) model. The mean high-pass barotropic kinetic energy is 1.40 PJ in the global model and 0.71 PJ in the regional model. The barotropic energy at the M2 frequency is 1.33 PJ in the global model and 0.57 PJ in the regional model. The spring/neap tide with period 13.66 days is the dominant signal in the barotropic energy inventory. (b) The high-pass baroclinic kinetic energy inventory for the global (blue line) and regional (red line) model. The yellow and purple lines are the same as plotted in a, and demonstrate how the baroclinic energy is approximately 2–3 days lag-correlated with the barotropic kinetic energy at the M2 frequency. The mean high-pass baroclinic kinetic energy is 1.79 PJ in the global model and 0.71 PJ in the regional model.
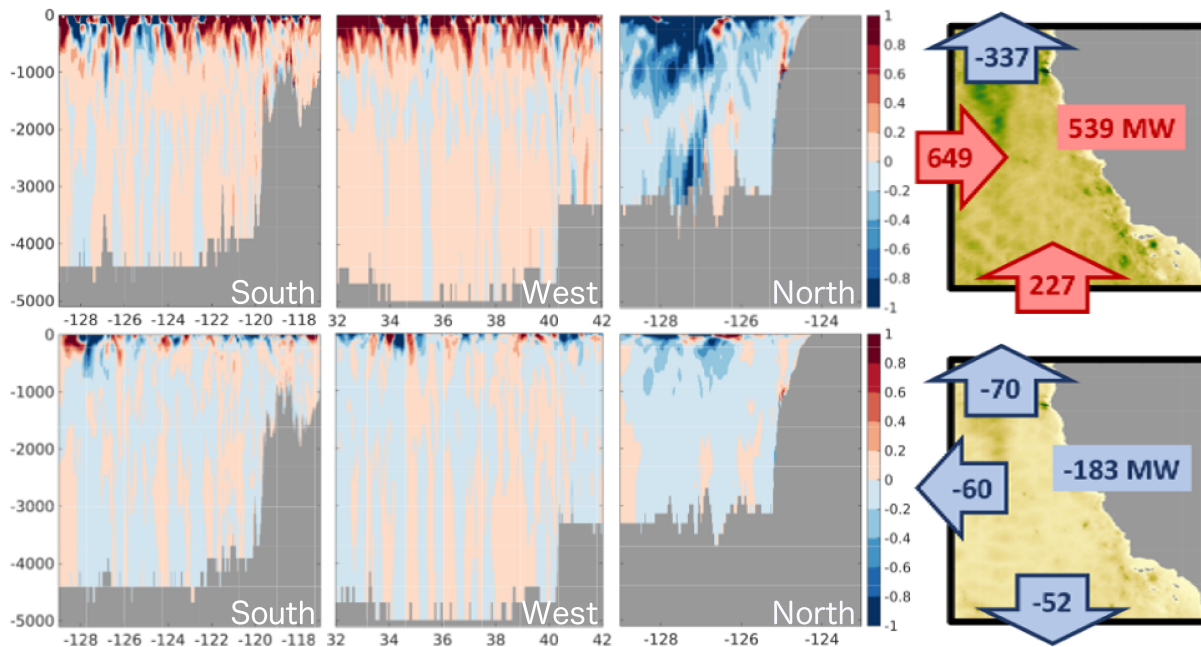
Figure 7. The energy flux calculated along three boundaries: southern (left), western (middle), and northern (right) boundaries, with the convention that positive values imply an energy flux into the domain and negative values imply a flux out of the domain. The upper panels are for the global simulation, and the bottom panels are for the regional simulation. The panels on the far right show the net results for the global and regional simulations. The domain-integrated energy fluxes give a 539 MW gain (1 MW= 10^6 W) for the global simulation and add a 183 MW loss for the regional simulation.

regional model are equivalent, yet in the global model the high-pass baroclinic energy is 0.39 PJ larger than the high-pass barotropic energy. The open boundary conditions for the regional model are only forced with mesoscale structure and barotropic tides. We hypothesize that the enhanced energy in the global model is due to internal wave energy propagating into the region, and in this subsection we consider the energy flux through the analysis domain boundaries.

The internal wave energy flux at the analysis domain boundaries can be quantified from the conservation of energy equation as $F_E = \langle \mathbf{u}'p' \rangle$, where the primed quantities are associated with high-frequency waves and $\langle \cdot \rangle$ represents time averaging and depth integration (Nash et al., 2005). The internal wave-induced perturbation baroclinic pressure is calculated as $p' = p - \bar{p} - p_{bt}$, and velocity as $\mathbf{u}' = \mathbf{u} - \bar{\mathbf{u}} - \mathbf{u}_{bt}$, where the overline denotes the low-pass component calculated with a 24-hr running mean and p_{bt} and $\mathbf{u}_{bt}$ are the barotropic fields such that the vertical integral of p' and $\mathbf{u}'$ vanish.

The domain-integrated wave energy flux convergence, $-\nabla \cdot \langle \mathbf{u}'p' \rangle$, reduces to

$$F_E = \int dx \langle v'p' \rangle_{south} - \int dx \langle v'p' \rangle_{north} + \int dy \langle u'p' \rangle_{west}. \tag{1}$$

Figure 7 shows the energy flux through the three open boundaries. In the global simulation 227 MW of internal wave energy fluxes in through the southern boundary and 649 MW through the western boundary. Meanwhile 337 MW of energy leaves through the northern boundary, likely due to the proximity of the Mendocino ridge generation site. Overall the boundaries act as a 539 MW net *source* of internal wave energy for the domain. As expected in the regional domain, the boundaries only act as a sink of internal wave energy, with 52 MW fluxed out through the southern boundary, 60 MW through the western boundary, and 70 MW through the northern boundary. Thus, the boundaries act as a net *sink* of 183 MW of internal wave energy for the regional domain.

The 539 MW influx for the global domain versus the 183 MW outflux for the regional domain reveals a net difference of 722 MW of power. Given the identical numerics in the models we expect the local sources and sinks of high-pass baroclinic energy to have similar rates. The primary local source is conversion from the barotropic tides. While the baroclinic high-pass energy was found to equilibrate to the magnitude of the barotropic high-pass energy in the regional domain, the baroclinic high-pass energy was 0.39 PJ higher

than the barotropic high-pass energy in the global domain. We hypothesize that the source of this excess energy is due to the remote forcing energy source. Accounting for this 0.39 PJ difference with a boundary flux difference of 722 MW implies a baroclinic wave energy dissipation time in the domain of 6.3 days. In other words, a 6.3 day time scale for the energy sink would allow a 722 MW influx to accumulate an excess 0.39 PJ in the domain over this time.

In section 3.5 we found that the analysis-domain-integrated high-pass baroclinic energy lagged the high-pass barotropic energy by approximately 1.9 days for the regional model and 2.8 days for the global model. Here we estimated an energy dissipation time of approximately 6.3 days. We can check the consistency of these findings using a simple integrated baroclinic energy budget that assumes temporal changes in energy, $\partial E/\partial t$, result from a source term, and a damping term proportional to domain energy, rE. Here $1/r$ denotes the dissipation time scale of 6.3 days, and the source term here oscillates with the 13.66 day spring/neap tidal period (Figure 6). Thus,

$$\partial E/\partial t + rE = Ae^{-i\omega t}, \tag{2}$$

where $\omega = 2\pi/13.66$. The solution is

$$E = A/(-i\omega + r)e^{-i\omega t} = A(i\omega + r)/(\omega^2 + r^2)e^{-i\omega t}, \tag{3}$$

revealing a phase shift of $\phi = \arctan(\omega/r) = 71° = 2.7$ days. This is consistent with the 2–3 day (i.e., approximately 65°) lag response of the baroclinic energy to the 13.66 day period spring/neap tide.

4. Conclusions and Discussion

Regional models are commonly forced at their open boundaries with mesoscale and larger balanced features, as well as with barotropic tides. To our knowledge at time of writing, we are unaware of realistic regional models being forced at the boundaries with internal waves. In this work we have compared the statistics of a global and regional model with the same resolution and numerics. Both models have barotropic tides consistent with observations, though the global model overestimates the M2 amplitude by about 30% and the regional model underestimates the M2 amplitude by about 10%. The global model has a steric height power spectrum consistent with mooring observations. The regional model has far less energy at superinertial nontidal frequencies (e.g., frequencies greater than 1.1 cycles per day at the CCE1 mooring and 1.2 cycles per day at the MBARI-M2 mooring). Regarding wavenumber statistics, the regional model is more consistent with the daily averaged global model, again demonstrating that the internal wave energy is low. Similarly, we find the variance of vertical velocity to be much larger in the global domain. An important exception, however, is in the sheltered SCB where the w variance is similar in both models.

The barotropic tide to internal tide energy transfer is theorized to scale linearly as $E \sim KE_b N_b kh^2$ where KE_b is the barotropic tidal energy, N_b is the buoyancy frequency near the seafloor, and the wavenumber, k, and amplitude, h, of the topography together characterize the bottom roughness or slope (Jayne & St. Laurent, 2001; St. Laurent et al., 2002). In assessing the domain kinetic energy, we found the global model barotropic energy to be 2.0 times larger than that of the regional domain. Most of the barotropic energy is associated with the M2 tide, and thus we attribute this difference to the fact that the directly forced M2 tidal energy is 2.3 times larger in the global domain. However, while the barotropic energy is 2.0 times larger in the global model, the global mean high-pass baroclinic energy is 2.5 times larger in the global model than the regional model. The simplest way to reconcile this difference is by acknowledging that the global model has many more source regions (i.e., more regions of complex topography with large kh^2), and the excess baroclinic energy is propagating into the analysis domain, consistent with Ponte and Cornuelle (2013).

The internal wave energy in the regional domain is locally forced. Internal waves are damped at the open boundaries by the restoring to the HYCOM+NCODA state. There is a net loss of 52, 60, and 70 MW of internal wave energy at the southern, western, and northern boundaries respectively. In stark contrast, the analysis domain boundaries act as a net internal wave energy source in the global model. Due to its proximity to the Mendocino Ridge, 337 MW of internal wave energy is exported across the northern boundary, but 227 MW comes in from the southern boundary and 649 MW comes in from the western boundary. This energy flux through the boundaries is hypothesized to originate from internal wave energy generated elsewhere in the global ocean, such as near Hawaii, in the western Pacific, and the Gulf of Alaska. The net result

is that the boundaries of the regional model act as a sink of 183 MW of internal wave energy while the global model analysis domain boundaries act as a source of 539 MW of internal wave energy. Assuming that the high-pass baroclinic kinetic energy dissipation time in the domain is approximately 6.3 days would allow this boundary flux difference to be responsible for the excess 0.39 PJ in the global domain.

There are numerous reasons to require regional models to reproduce the oceanic internal wave fields, either deterministically or statistically. Deterministic representation allows exact interpretation of ocean measurements at short space and time scales to the extent that internal waves are treated as signal instead of noise. Applications include acoustic propagation (Duda, 2017) and process experiments to quantify the interactions that produce the continuum spectrum. On the other hand, since internal waves are a primary driver of ocean turbulence, statistical representation in models allows reproduction of ocean physical and ecosystem dynamics (MacKinnon et al., 2017). However, internal waves travel thousands of kilometers, delivering energy to remote regions (Zhao et al., 2010). The work here suggests that these remotely forced waves, and the waves generated by their resulting interaction with the local topography, fill the continuum spectrum observed in the California Current System. We showed that a regional model without remote internal wave forcing was unable to achieve the steric height power spectra of a global run, despite the same numerics. Similarly, the SSH high-wavenumber energy was lower in the regional model.

The results here suggest that reproducing the observed internal wave continuum spectrum in regional models requires accounting for the internal wave energy flux at the open boundaries. An exception may occur in select domains, such as the SCB, that are isolated from remote internal wave forcing, but these will be special cases. Thus, we have identified a serious problem for regional modeling. Future work must establish methods for providing a realistic representation of internal wave energy fluxes at regional model open boundaries. Many possible solutions exist for a given modeling need. If only statistical representation is desired it is possible that stochastic boundary forcing with a given (Mode 1) vertical structure has the potential to offer a computationally inexpensive form of boundary forcing. If specific temporal phasing is required, that phase knowledge needs to be derived from either global models or oceanic observations. A next step is to diagnose the vertical and frequency structure of the energy flux in the global MITgcm model accounting for the boundary flux shown in Figure 7. It is possible that much of this flux can be accounted for by a very limited number of vertical mode structures and (tidal) frequencies, enabling forcing to be prescribed as has been done for theoretical solutions (e.g., Griffiths & Grimshaw, 2007; Lahaye & Llewellyn Smith, 2020) and with amplitude and phasing derived from observations (Zhao et al., 2019) or global models. For some domains it may be necessary to force with the full continuum spectrum, requiring boundary forcing to be prescribed at high-frequency from global models. However, availability and accuracy of this global model output may prove problematic. Finally, in a four-dimensional variational (4dVar) data assimilation framework with sufficient constraints, it may be possible to solve for the internal wave fluxes at the open boundaries. An additional challenge that will arise is the requirement to minimize spurious turbulence at the open boundary when these additional internal wave fluxes are implemented. Determining best practices for a given application will require model experimentation with accompanying validation of the energy flux composition.

References

Acton, C., Bachman, N., Semenov, B., & Wright, E. (2018). A look towards the future in the handling of space science mission geometry. *Planetary and Space Science*, *150*, 9–12.

Adcroft, A., Hill, C., & Marshall, J. (1997). Representation of topography by shaved cells in a height coordinate ocean model. *Monthly Weather Review*, *125*(9), 2293–2315.

Amante, C., & Eakins, B. W. (2009). ETOPO1 1 arc-minute global relief model: Procedures, data sources and analysis. NOAA Technical Memorandum NESDIS NGDC-24.

Arbic, B. K., Alford, M. H., Ansong, J. K., Buijsman, M. C., Ciotti, R. B., Farrar, J. T., et al. (2018). Primer on global internal tide and internal gravity wave continuum modeling in HYCOM and MITgcm. *New Frontiers in Operational Oceanography*, 307–392.

Bonnefond, P., Laurain, O., Exertier, P., Boy, F., Guinle, T., Picot, N., et al. (2018). Calibrating the SAR SSH of Sentinel-3A and CryoSat-2 over the Corsica facilities. *Remote Sensing*, *10*, 92. https://doi.org/10.3390/rs10010092

Chereskin, T. K., Rocha, C. B., Gille, S. T., Menemenlis, D., & Passaro, M. (2019). Characterizing the transition from balanced to unbalanced motions in the Southern California Current. *Journal of Geophysical Research: Oceans*, *124*, 2088–2109. https://doi.org/10.1029/2018JC014583

Daru, V., & Tenaud, C. (2004). High order one-step monotonicity-preserving schemes for unsteady compressible flow calculations. *Journal of Computational Physics*, *193*(2), 563–594. https://doi.org/10.1016/j.jcp.2003.08.023

Dibarboure, G., Boy, F., Desjonqueres, J. D., Labroue, S., Lasne, Y., Picot, N., et al. (2014). Investigating short-wavelength correlated errors on low-resolution mode altimetry. *Journal of Atmospheric and Oceanic Technology*, *31*(6), 1337–1362. https://doi.org/10.1175/JTECH-D-13-00081.1

Dibarboure, G., & Morrow, R. (2016). Value of the Jason-1 geodetic phase to study rapid oceanic changes and importance for defining a Jason-2 geodetic orbit. *Journal of Atmospheric and Oceanic Technology*, *33*(9), 1913–1930. https://doi.org/10.1175/JTECH-D-16-0015.1

Divins, D., & Metzger, D. (2008). NGDC coastal relief model, Southern California 30 arc-second bathymetry map. Download provided by the Southern California Coastal Ocean Observing System. http://sccoos.org/data/bathy

Duda, T. F. (2017). Modeling and forecasting ocean acoustic conditions. *Journal of Marine Research*, *75*(3), 435–457.

Egbert, G. D., & Erofeeva, S. Y. (2002). Efficient inverse modeling of barotropic ocean tides. *Journal of Atmospheric and Oceanic Technology*, *19*(2), 183–204. https://doi.org/10.1175/1520-0426(2002)019<0183:EIMOBO>2.0.CO;2

Fairall, C., Bradley, E. F., Hare, J., Grachev, A., & Edson, J. (2003). Bulk parameterization of air–sea fluxes: Updates and verification for the COARE algorithm. *Journal of climate*, *16*(4), 571–591.

Ferrari, R., & Wunsch, C. (2010). The distribution of eddy kinetic and potential energies in the global ocean. *Tellus A: Dynamic Meteorology and Oceanography*, *62*(2), 92–108.

Flexas, M. M., Schodlok, M. P., Padman, L., Menemenlis, D., & Orsi, A. H. (2015). Role of tides on the formation of the Antarctic Slope Front at the Weddell-Scotia Confluence. *Journal of Geophysical Research: Oceans*, *120*, 3658–3680. https://doi.org/10.1002/2014JC010372

Flexas, M. M., Thompson, A. F., Torres, H. S., Klein, P., Farrar, J. T., Zhang, H., & Menemenlis, D. (2019). Global estimates of the energy transfer from the wind to the ocean, with emphasis on near-inertial oscillations. *Journal of Geophysical Research: Oceans*, *124*, 5723–5746. https://doi.org/10.1029/2018JC014453

Fox-Kemper, B., & Menemenlis, D. (2013). Can large eddy simulation techniques improve mesoscale rich ocean models?*Ocean modeling in an eddying regime* (pp. 319–337). Washington, DC: American Geophysical Union (AGU). https://doi.org/10.1029/177GM19

Garrett, C., & Munk, W. (1975). Space-time scales of internal waves: A progress report. *Journal of Geophysical Research*, *80*, 291–297.

Good, S. A., Martin, M. J., & Rayner, N. A. (2013). En4: Quality controlled ocean temperature and salinity profiles and monthly objective analyses with uncertainty estimates. *Journal of Geophysical Research: Oceans*, *118*, 6704–6716. https://doi.org/10.1002/2013JC009067

Griffiths, S. D., & Grimshaw, R. H. J. (2007). Internal tide generation at the continental shelf modeled using a modal decomposition: Two-dimensional results. *Journal of Physical Oceanography*, *37*(3), 428–451. https://doi.org/10.1175/JPO3068.1

Hodur, R. M. (1997). The Naval Research Laboratory's Coupled Ocean/Atmosphere Mesoscale Prediction System (COAMPS). *Monthly Weather Review*, *125*(7), 1414–1430.

Hoteit, I., Cornuelle, B., Köhl, A, & Stammer, D. (2005). Treating strong adjoint sensitivities in tropical eddy-permitting variational data assimilation. *Quarterly Journal of the Royal Meteorological Society*, *131*(613), 3659–3682.

Hughes, K. G., & Klymak, J. M. (2019). Tidal conversion and dissipation at steep topography in a channel poleward of the critical latitude. *Journal of Physical Oceanography*, *49*(5), 1269–1291.

Jayne, S. R., & St. Laurent, L. C. (2001). Parameterizing tidal dissipation over rough topography. *Geophysical Research Letters*, *28*(5), 811–814. https://doi.org/10.1029/2000GL012044

Johnston, T. M. S., & Rudnick, D. L. (2015). Trapped diurnal internal tides, propagating semidiurnal internal tides, and mixing estimates in the California Current System from sustained glider observations, 2006–2012. *Deep Sea Research Part II: Topical Studies in Oceanography*, *112*, 61–78. https://doi.org/10.1016/j.dsr2.2014.03.009

Kilpatrick, T., Xie, S.-P., Miller, A. J., & Schneider, N. (2018). Satellite observations of enhanced chlorophyll variability in the Southern California Bight. *Journal of Geophysical Research: Oceans*, *123*, 7550–7563. https://doi.org/10.1029/2018JC014248

Klymak, J. M., Simmons, H. L., Braznikov, D., Kelly, S., MacKinnon, J. A., Alford, M. H., et al. (2016). Reflection of linear internal tides from realistic topography: The Tasman continental slope. *Journal of Physical Oceanography*, *46*(11), 3321–3337. https://doi.org/10.1175/JPO-D-16-0061.1

Lahaye, N., & Llewellyn Smith, S. G. (2020). Modal analysis of internal wave propagation and scattering over large-amplitude topography. *Journal of Physical Oceanography*, *50*, 305–321. https://doi.org/10.1175/JPO-D-19-0005.1

Large, W. G., McWilliams, J. C., & Doney, S. C. (1994). Oceanic vertical mixing: A review and a model with a nonlocal boundary layer parameterization. *Reviews of Geophysics*, *32*(4), 363–403.

Li, Z., Wang, J., & Fu, L.-L. (2019). An observing system simulation experiment for ocean state estimation to assess the performance of the SWOT mission: Part 1a twin experiment. *Journal of Geophysical Research: Oceans*, *124*, 4838–4855. https://doi.org/10.1029/2018JC014869

MacKinnon, J. A., Zhao, Z., Whalen, C. B., Waterhouse, A. F., Trossman, D. S., Sun, O. M., et al. (2017). Climate process team on internal wave-driven ocean mixing. *Bulletin of the American Meteorological Society*, *98*(11), 2429–2454. https://doi.org/10.1175/BAMS-D-16-0030.1

Marchesiello, P., McWilliams, J. C., & Shchepetkin, A. (2001). Open boundary conditions for long-term integration of regional oceanic models. *Ocean Modelling*, *3*(1), 1–20. https://doi.org/10.1016/S1463-5003(00)00013-5

Marsaleix, P., Auclair, F., & Estournel, C. (2006). Considerations on open boundary conditions for regional and coastal ocean models. *Journal of Atmospheric and Oceanic Technology*, *23*(11), 1604–1613. https://doi.org/10.1175/JTECH1930.1

Morrow, R., Fu, L.-L., D'Ovidio, F., & Farrar, J. T. (2019). Scientists invited to collaborate in satellite missions debut. *EOS*, *100*. https://doi.org/10.1029/2019EO110423

Musgrave, R. C., Pinkel, R., MacKinnon, J., Mazloff, M. R., & Young, W. (2016). Stratified tidal flow over a tall ridge above and below the turning latitude. *Journal of Fluid Mechanics*, *793*, 933–957.

Nash, J. D., Alford, M. H., & Kunze, E. (2005). Estimating internal wave energy fluxes in the ocean. *Journal of Atmospheric and Oceanic Technology*, *22*(10), 1551–1570.

Nikurashin, M., & Legg, S. (2011). A mechanism for local dissipation of internal tides generated at rough topography. *Journal of Physical Oceanography*, *41*(2), 378–395.

Passaro, M., Dinardo, S., Quartly, G. D., Snaith, H. M., Benveniste, J., Cipollini, P., & Lucas, B. (2016). Cross-calibrating ALES, Envisat and Cryosat-2 Delay Doppler: A coastal altimetry study in the Indonesian seas. *Advances in Space Research*, *58*(3), 289–303. https://doi.org/10.1016/j.asr.2016.04.011

Pawlowicz, R., Beardsley, B., & Lentz, S. (2002). Classical tidal harmonic analysis including error estimates in MATLAB using T_TIDE. *Computers & Geosciences*, *28*(8), 929–937. https://doi.org/10.1016/S0098-3004(02)00013-4

Polzin, K. (2004). A heuristic description of internal wave dynamics. *Journal of Physical Oceanography*, *34*(1), 214–230. https://doi.org/10.1175/1520-0485(2004)034<0214:AHDOIW>2.0.CO;2

Ponte, A. L., & Cornuelle, B. D. (2013). Coastal numerical modelling of tides: Sensitivity to domain size and remotely generated internal tide. *Ocean Modelling*, *62*, 17–26. https://doi.org/10.1016/j.ocemod.2012.11.007

Qiu, B., Chen, S., Klein, P., Torres, H., Wang, J., Fu, L., & Menemenlis, D. (2020). Reconstructing upper-ocean vertical velocity field from sea surface height in the presence of unbalanced motion. *Journal of Physical Oceanography*, *50*, 55–79. https://doi.org/10.1175/JPO-D-19-0172.1

Qiu, B., Chen, S., Klein, P., Wang, J., Torres, H., Fu, L.-L., & Menemenlis, D. (2018). Seasonality in transition scale from balanced to unbalanced motions in the world ocean. *Journal of Physical Oceanography*, *48*, 591–605. https://doi.org/10.1175/JPO-D-17-0169.1

Rocha, C. B., Chereskin, T. K., Gille, S. T., & Menemenlis, D. (2016). Mesoscale to submesoscale wavenumber spectra in Drake Passage. *Journal of Physical Oceanography*, *46*(2), 601–620. https://doi.org/10.1175/JPO-D-15-0087.1

Rudnick, D. L., Zaba, K. D., Todd, R. E., & Davis, R. E. (2017). A climatology of the California Current System from a network of underwater gliders. *Progress in Oceanography*, *154*, 64–106. https://doi.org/10.1016/j.pocean.2017.03.002

Savage, A. C., Arbic, B. K., Alford, M. H., Ansong, J. K., Farrar, T. J., Menemenlis, D., et al. (2017). Spectral decomposition of internal gravity wave sea surface height in global models. *Journal of Geophysical Research: Oceans*, *122*, 7803–7821. https://doi.org/10.1002/2017JC013009

St. Laurent, L. C., Simmons, H. L., & Jayne, S. R. (2002). Estimating tidally driven mixing in the deep ocean. *Geophysical Research Letters*, *29*(23), 21–1–21–4. https://doi.org/10.1029/2002GL015633

Su, Z., Wang, J., Klein, P., Thompson, A. F., & Menemenlis, D. (2018). Ocean submesoscales as a key component of the global heat budget. *Nature Communications*, *9*(1), 775. https://doi.org/10.1038/s41467-018-02983-w

Torres, H. S., Klein, P., Menemenlis, D., Qiu, B., Su, Z., Wang, J., et al. (2018). Partitioning ocean motions into balanced motions and internal gravity waves: A modeling study in anticipation of future space missions. *Journal of Geophysical Research: Oceans*, *123*, 8084–8105. https://doi.org/10.1029/2018JC014438

Vergara, O., Morrow, R., Pujol, I., Dibarboure, G., & Ubelmann, C. (2019). Revised global wave number spectra from recent altimeter observations. *Journal of Geophysical Research: Oceans*, *124*, 3523–3537. https://doi.org/10.1029/2018JC014844

Verron, J., Bonnefond, P., Aouf, L., Birol, F., Bhowmick, S. A., Calmant, S., et al. (2018). The benefits of the Ka-band as evidenced from the SARAL/AltiKa altimetric mission: Scientific applications. *Remote Sensing*, *10*, 163. https://doi.org/10.3390/rs10020163

Wang, J., Fu, L.-L., Qiu, B., Menemenlis, D., Farrar, J. T., Chao, Y., et al. (2018). An observing system simulation experiment for the calibration and validation of the surface water ocean topography sea surface height measurement using in situ platforms. *Journal of Atmospheric and Oceanic Technology*, *35*(2), 281–297.

Wang, J., Fu, L.-L., Torres, H. S., Chen, S., Qiu, B., & Menemenlis, D. (2019). On the spatial scales to be resolved by the surface water and ocean topography Ka-band radar interferometer. *Journal of Atmospheric and Oceanic Technology*, *36*(1), 87–99. https://doi.org/10.1175/JTECH-D-18-0119.1

Zhao, Z., Alford, M. H., MacKinnon, J. A., & Pinkel, R. (2010). Long-range propagation of the semidiurnal internal tide from the Hawaiian Ridge. *Journal of Physical Oceanography*, *40*(4), 713–736.

Zhao, Z., Wang, J., Menemenlis, D., Fu, L.-L., Chen, S., & Qiu, B. (2019). Decomposition of the multimodal multidirectional M2 internal tide field. *Journal of Atmospheric and Oceanic Technology*, *36*(6), 1157–1173. https://doi.org/10.1175/JTECH-D-19-0022.1